Ann. Geophys., 34, 529–541, 2016
www.ann-geophys.net/34/529/2016/
doi:10.5194/angeo-34-529-2016

Annales Geophysicae
Open Access

A multi-platform investigation of midlatitude sporadic E and its ties to E–F coupling and meteor activity

Joseph Helmboldt

US Naval Research Laboratory, Code 7213, 4555 Overlook Ave. SW, Washington, DC 20375, USA

Correspondence to: Joseph Helmboldt (joe.helmboldt@nrl.navy.mil)

Received: 4 February 2016 – Revised: 20 April 2016 – Accepted: 24 April 2016 – Published: 10 May 2016

Abstract. This paper describes the results of a multi-platform observing campaign aimed at studying midlatitude sporadic E (E_s) and associated ionospheric phenomena. The assets used were the digisonde in Boulder, Colorado; the first station of the Long Wavelength Array, LWA1, in New Mexico; the transmitters of the radio station WWV in Colorado; and 61 continuously operating GPS receivers between LWA1 and WWV. The results show that southwestward-directed medium-scale traveling ionospheric disturbances (MSTIDs) were substantially more prevalent when E_s was detected. The amplitudes of these correlate with a plasma frequency up to about 4.5 MHz. For $f_\mathrm{p} \gtrsim 5$ MHz, the MSTIDs become significantly weaker and basically vanish above ~ 6.5 MHz. The prevalence of meteor trail reflections observed with LWA1 also correlates with f_p up to about 4.5 MHz; above this limit, the relationship exhibits a significant turnover. The observed intensity of coherent backscatter from E_s field-aligned irregularities (FAIs) also correlates with inferred plasma frequency. However, this trend continues to higher frequencies with a peak near 6 MHz, followed by a much more subtle turnover. The reflected power from E_s structures observed with LWA1 is significantly more correlated on spatial scales between 10 and 40 km. The magnitude of this correlation increases with f_p up to $\sim$ 6 MHz, above which it drops. These results are consistent with the following: (1) southwestward-directed MSTIDs are produced via E–F coupling; (2) this coupling is stronger when the E_s layer, seeded by meteor ablation, is more dense; (3) the coupling is substantially diminished for E_s layers harboring extremely dense structures ($f_\mathrm{p} \gtrsim 5$ MHz).

Keywords. Ionosphere (ionospheric irregularities; midlatitude ionosphere; plasma waves and instabilities)

1 Introduction

Midlatitude sporadic E (E_s) is a well-known ionospheric phenomenon. As the name suggests, E_s appears at E-region heights ($\sim$100–120 km) intermittently throughout the year, most prominently during summer nighttime, especially in the Northern Hemisphere (e.g., Arras et al., 2010). Fundamental to its existence are tidally induced, zonal wind shears that compress metallic ions into a relatively thin region via a combination of ion–neutral collision-generated currents and $E \times B$ force. (For a much more thorough review of the processes involved, see Haldoupis, 2012). Consequently, the deposition of heavy ions within the E region by ablating meteors may play a key role in E_s formation. Interestingly, some investigations found no observational evidence of a correlation between meteor activity and E_s (e.g., Baggaley and Steel, 1984; Whitehead, 1989). However, some instances of positive correlation between E_s and meteor activity have been observed (e.g., Haldoupis et al., 2007), and there is some indication that the occurrence of E_s is enhanced during meteor showers (Chandra et al., 2001; Yellaiah et al., 2001).

While these thin E_s structures are oftentimes spoken of in terms of “layers”, it has been known for decades that E_s is, in fact, quite patchy (e.g., Miller and Smith, 1978). In particular, ionograms demonstrate that the maximum frequency reflected by E_s (foEs) is nearly always larger than the so-called blanketing frequency (fbEs), the frequency below which reflections from higher altitudes are not detected.

The spotty nature of E_s is also related to a phenomenon seen within radar observations, referred to as quasi-periodic (QP) echoes. QP echoes typically appear at intervals of roughly 10–15 min, spaced by $\sim$10 km from one another (e.g., Bowman, 1989; Pan and Tsunoda, 1998; Hysell and Burcham, 1999). These structures are thought to arise through ion–neutral coupling within the lower ionosphere when turbulent, billowy structures form within the neutral gas due to Kelvin–Helmholtz (K–H) instabilities associated with the same zonal wind shears that form the E_s layers (e.g., Larsen, 2000; Bernhardt, 2002; Hysell et al., 2012). Alternatively, it has been demonstrated that structures on similar scales can be produced by an instability resulting from the wind shears that form E_s layers that favors the growth of perturbations that are aligned northwest to southeast in the Northern Hemisphere (Cosgrove and Tsunoda, 2002). There is some observational evidence from radar imaging for southwestward-propagating wavelike structures traced by E_s irregularities (e.g., Hysell et al., 2004; Larsen et al., 2007). However, other propagation directions or orientations were also observed, indicating that other structure-forming mechanisms must also be at play. It has been shown that the polarized electric fields that fuel the Cosgrove and Tsunoda (2002) instability can remotely interact with similar fields formed by the Perkins instability (Perkins, 1973) in the F region, using both physical arguments (Cosgrove et al., 2004) and simulations (Cosgrove, 2007; Yokoyama et al., 2009). This E–F coupling instability has been posited to be the origin of southwestward-propagating traveling ionospheric disturbances (TIDs) seen prominently during summer nighttime in the Northern Hemisphere (e.g., Hernández-Pajares et al., 2006; Tsugawa et al., 2007). The growth rate of the Perkins instability alone has been noted to be too low to generate these F-region wavefronts, making the coupled E–F instability, which has a larger growth rate by a factor of a few (Cosgrove et al., 2004), a more likely candidate. The fact that these TIDs are often coincident in time with E_s (e.g., Helmboldt, 2012) is consistent with this hypothesis.

The details of E–F coupling are unclear as elucidative observations remain scant (for a review, see Cosgrove, 2013). In particular, the complicated state of E_s is far from the idealized initial layer used in calculations (e.g., Cosgrove et al., 2004; Yokoyama et al., 2009). There is some observational evidence that suggests that E–F coupling is disrupted when higher densities are present within the E_s layer (Helmboldt, 2012), consistent with some simulated results (Cosgrove, 2007). However, it is not clear if these higher densities are caused by clumpy structures associated with, for example, K–H instabilities or with E_s layers that are simply nonuniform in nature.

This paper presents the results of an observing campaign conducted in the summer of 2013, intended to shed light on these open questions. The analysis presented here is a combination of data from different remote sensing platforms used to simultaneously monitor for and measure the properties of E_s as well as meteor trail activity and TIDs in the form of wavelike fluctuations in total electron content (TEC). The sensors (and transmitters) involved and the observations made are described in Sect. 2. The results are presented in Sect. 3, and their implications are discussed in more detail in Sect. 4.

2 Instruments, observations, and processing

The E_s investigation presented here relies on what are essentially three independent remote sensing platforms. They are used together to monitor the same region (Colorado and northern New Mexico) for E_s, meteor trails, and medium-scale TIDs (MSTIDs; wavelengths $\sim$100–500 km). The details of the instruments involved and the observations conducted are given below.

2.1 LWA1, WWV, FAIs, and meteor trails

At the heart of this program are six observing runs conducted in summer 2013 with the first station of the Long Wavelength Array, LWA1. A 100 m diameter array of 256 bent-dipole antennas, LWA1 is the first station within what is intended to be a larger array of more than 50 similar stations spread throughout New Mexico for high-angular-resolution imaging of cosmic sources in the HF/VHF (high-frequency–very high-frequency) regime. While the future of the full LWA is uncertain, LWA1 is currently run as a stand-alone observatory (at $\phi = 34.070°$ N, $\lambda = 107.628°$ W), capable of operating within the 10–88 MHz range in one of three modes. These include a relatively wide-band (16 MHz) beam-forming mode and two transient buffer (TB) modes that each capture the signals from individual antennas, allowing for all-sky imaging after the fact. For more details of the LWA1 radio telescope, see Hicks et al. (2012), Taylor et al. (2012), and Ellingson et al. (2013).

It is the all-sky TB modes that have the greatest potential for passive radar, the exploitation of transmitters of opportunity to illuminate a given target. In this case, the "targets" are E_s layers and meteor trails. Specifically, Helmboldt et al. (2013) showed that the HF transmitters of the NIST radio station WWV near Ft. Collins, Colorado (see Fig. 1), could be used with LWA1's TB modes to probe the ionosphere. WWV broadcasts the time at 2.5, 5, 10, 15, and 20 MHz, including a 5 ms pulse at the beginning of each UT second (Nelson et al., 2005) that can be used for ranging. The frequency overlap between LWA1 and WWV is thus at 10, 15, and 20 MHz. Sky waves from WWV are often observed at 10 MHz, either from the lower F region or from E_s. The geometry is such that 15 and 20 MHz sky waves can only originate from dense, low-altitude ($\sim$ 100 km) plasma, i.e., E_s.

The LWA1+WWV passive radar works with both the wide-band and narrow-band TB modes (TBW and TBN, respectively). The TBW mode produces a 61 ms capture of the raw signal from each antenna, allowing access to the full band (10–88 MHz) for all-sky imaging. Unfortunately, the time it takes to write this data to disk (nearly 10 GB for one capture) is so long ($\sim$ 5 min) that the duty cycle is rather low. With the TBN mode, each antenna's signal is tuned to a selected frequency with 100 kHz of bandwidth ($\sim$ 70 kHz is actually usable) that can be run continuously for up to 20 h (when the available disks fill up).

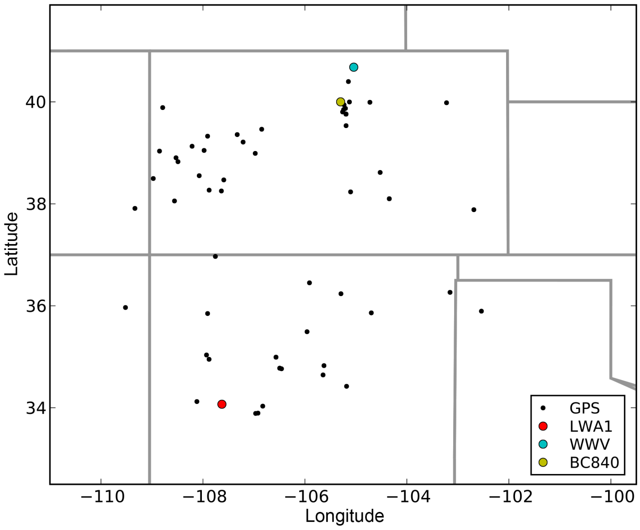

Figure 1. Locations of the remote sensing platforms used in this study including 61 continuously operating GPS receivers (black points), the Boulder digisonde (BC840; yellow), LWA1 (red), and the WWV transmitters (cyan).

Using either mode, the antenna outputs are processed to isolate the WWV pulse at different group paths and are then used to generate image cubes that show the received pulse power over the entire visible sky at each group path. From these, one can measure the altitude, azimuth, and group path of any detected sky wave. Consequently, with TBW captures, one can simultaneously measure sky wave properties at 10, 15, and 20 MHz, but only every 5–6 min. Conversely, TBN data allows one to do the same with 1 s sampling, but only at a single frequency. In either case, the combined radar is quite useful for observing E_s, especially at 15 and 20 MHz. In particular, the all-sky imaging capability and bistatic nature of the LWA1+WWV system manifest a probe of E_s structures that can pinpoint their horizontal positions to a precision as good as 1 km over a relatively large area (∼100 km wide and several hundred kilometers long). This is discussed at greater length by Helmboldt et al. (2013).

All-sky imaging with LWA1 can similarly be used to detect, locate, and characterize VHF transmissions backscattered by field-aligned irregularities (FAIs) and/or meteor trails. For the right bistatic configuration, ionospheric structures with small-scale irregularities (half the observing wavelength) aligned along magnetic field lines will Bragg scatter signals to the receiver array. In addition to FAIs, meteor trails collectively act as a persistent source of VHF backscatter. As meteors ablate in the lower ionosphere (∼ 80–100 km), they produce dense, transient structures that are nearly linear and can produce specular reflections of VHF radiation.

For LWA1, there is a relatively nearby and powerful analog TV transmitter located in Ciudad Juárez, Mexico, roughly 280 km south-southeast of LWA1. According to the Federal Communications Commission (FCC), the effective radiative power (ERP) of this nondirectional, horizontally polarized transmitter (call sign XEPM) is 9.5 kW. It broadcasts on "Channel 2" with a very narrow-band, amplitude-modulated video carrier at 55.25 MHz. Helmboldt et al. (2014) demonstrated that using this video carrier, $\gtrsim$ 9000 meteor trails can be detected and located on the sky per hour using LWA1 TBN data. This is well over an order of magnitude larger that the count rates achieved with more commonly utilized dipole-based, all-sky meteor radars such as the Canadian Meteor Orbit Radar (CMOR) arrays and All-Sky Interferometric Meteor Radar (SKiYMET) systems (∼ 100–300 h^{-1} near local midnight; Hocking et al., 2001; Webster et al., 2004). The data processing and imaging pipeline developed by Helmboldt et al. (2014) can also be used to identify and track FAIs along arcs in the sky north of the array where backscattering is possible. At 55.25 MHz, LWA1 has an angular resolution on the sky of about 3.1°. This is comparable to the azimuthal resolution (∼ 4°) of the 30 MHz imaging radar deployed in St Croix (US Virgin Islands) in 2002 and used to study backscatter from E_s irregularities over Puerto Rico, i.e., at a latitude not dissimilar to LWA1 (see, e.g., Hysell et al., 2004; Larsen et al., 2007).

For FAI and meteor trail observing alone, the complementary TBW mode offers no apparent advantages over the TBN mode. However, for the purpose of examining how meteor activity impacts E_s while also detecting and characterizing FAIs associated with E_s, the extremely wide bandwidth of the TBW mode offers a singularly useful kind of data set. With a series of TBW captures, one can simultaneously observe specular meteor trail reflections, E_s reflections of WWV pulses at 10, 15, and 20 MHz, and VHF backscatter from E_s FAIs. With this motivation, time was obtained with LWA1 for six observing runs in 2013 during summer nighttime when E_s is most prevalent. Specifically, each run consisted of a series of 80 TBW captures spaced by 6 min from 03:00 to 11:00 UT (roughly 19:50 to 03:50 local time). The observations were conducted on 23 June; 21 July; 4, 13, and 21 August; and 1 September (or, as days of the year, on DOY 174, 202, 216, 225, 233, and 244).

The data were processed with python-based software, including the LWA Software Library (LSL; Dowell et al., 2012), to produce all-sky or group path image cubes using WWV pulses at 10, 15, and 20 MHz. These cubes were analyzed according to Helmboldt et al. (2013) to measure the sky location and group path of each WWV reflection. To monitor for FAIs and meteor trails, all-sky images were also produced within 45 frequency channels, centered at 55.25 MHz and spaced by 16.33 Hz, covering a range in Doppler speed of about ±1000 $\mathrm{m\,s^{-1}}$ with a resolution of roughly 90 $\mathrm{m\,s^{-1}}$. To convert these spectral images into all-sky maps of backscattered signals, the image for each channel was normalized by its noise level, estimated with the median absolute deviation (MAD). These signal-to-noise (S/N) all-sky maps were then converted to a single peak S/N map for each TBW capture by simply computing the maximum S/N over all channels at each all-sky pixel. This was done to mitigate the effect of very bright meteor trails which artificially increase the noise within an image because of the sidelobes associated with the LWA1 beam. Because the video carrier signal is inherently quite narrow ($\sim$ 20–30 Hz), this typically only affects 1–3 channels near the Doppler frequency of a bright trail. Thus, this S/N-based approach allows fainter sources at significantly different Doppler frequencies to still be detected. A similar technique used to maximize meteor trail detections with TBN data is detailed in the Appendix of Helmboldt et al. (2013).

2.2 Boulder digisonde and GPS

Supplementing the LWA1 observations and data products are two additional remote sensing assets. The first is the digital ionosonde, or "digisonde", near Boulder, Colorado (station ID BC840). The location of BC840 relative to LWA1 and WWV is shown in Fig. 1. Ionogram data (frequencies, ranges, and amplitudes) were obtained for BC840 for the times during the LWA1 observations from the Digital Ionogram Database (DIDBase; Reinisch et al., 2004), except for 23 June (DOY: 174) when no BC840 data were available. From these, mean ionograms were produced within half-hour intervals during all but the first observing run. Visual inspection of these revealed the signature of E_s during many of the observations below virtual heights of 122 km.

The second asset is an array of continuously operating GPS receivers. These were chosen from the publicly accessible Continuously Operating Reference Station (CORS) (ftp://www.ngs.noaa.gov/cors/rinex/) and UNAVCO (ftp://data-out.unavco.org/pub/rinex/) databases. All stations from these repositories that were within 400 km of the midpoint between LWA1 and WWV were chosen so that they would cover roughly the same area as the LWA1+WWV radar (the separation between LWA1 and WWV is 770 km) and BC840. The 61 stations that meet this criterion are almost exclusively in Colorado and northern New Mexico; their exact locations are shown in Fig. 1.

Data for the GPS array were obtained in Receiver Independent Exchange (RINEX) format for the dates of the LWA1 observing run. These were processed with software available within the GPS Toolkit (GPSTk; Tolman et al., 2004) to generate relative slant TEC (STEC) time series for each receiver–satellite pair. To remove instrumental biasses and to focus on TEC fluctuations, these STEC time series were detrended according to Hernández-Pajares et al. (2006). Within this de-trending scheme, at each time step, the average between the time steps that are τ seconds before and after the time step is subtracted, where τ is a flexible timescale. This finite differencing method has the drawbacks of increasing the noise somewhat (by a factor of about $\sqrt{1.5} = 1.22$) and rendering the first and last τ seconds of each time series useless. However, the chief advantage is that it produces a predictable temporal frequency response: $2\sin^2(\pi\tau\nu)$, where ν is the temporal frequency. In other words, a TEC fluctuation with a period of ν^{-1} and amplitude A will have a modified amplitude $A' = 2A\sin^2(\pi\tau\nu)$ after de-trending is applied. Thus, the choice of τ allows one to tune the GPS data to a particular range of fluctuation periods or frequencies. This is especially important for the spectral analysis that will be used to characterize TIDs.

For each satellite, a three-dimensional Fourier analysis was performed over the array, with one temporal dimension and two spatial ones. For this, each de-trended STEC time series was broken into 30 min segments, overlapping with the mean ionograms produced with the BC840 data. Each segment was then analyzed according to Helmboldt and Intema (2014). This starts with a straightforward temporal discrete Fourier transform, followed by a specialized spatial Fourier analysis meant to deal with the consequences of the sparse and irregular nature of the GPS array that was used. This includes the incorporation of deconvolution techniques developed and thoroughly tested within the field of radio astronomy for the similar problem of generating synthesis images of cosmic sources with radio-frequency interferometers. These techniques mitigate the impact of high-frequency structures caused by the array geometry (i.e., sidelobes) as well as phase errors caused mainly by wavefront distortions and/or point-of-view effects that vary in magnitude over the array. See Helmboldt and Intema (2014) for a much more detailed description. The end product of this analysis is a power spectrum cube (again, one temporal frequency axis and two spatial frequency axes) of TEC fluctuations within each 30 min segment.

During the application of this process, different values for the de-trending timescale, τ, were tried. In the end, $\tau = 600$ s was adopted as it appeared to provide the optimum temporal frequency response for MSTIDs during the LWA1 observations, similar to what was found by Helmboldt et al. (2012) in the same geographic region. The analysis was also limited to times when the observed satellites were above 30° elevation to avoid biases resulting from extreme line-of-sight effects and to ensure that the area of the ionosphere being probed was reasonably similar to that observed with LWA1+WWV and BC840.

3 TIDs, meteors, and sporadic-E properties

To examine how southwestward-directed MSTIDs and levels of meteor activity relate to E_s, the data products described in Sect. 2 were combined to yield average representations according to E_s properties as measured with LWA1+WWV and BC840. As an initial trial, the GPS-based TEC fluctuation spectrum cubes were divided into four groups: two groups with concurrent E_s detections from either LWA1 or

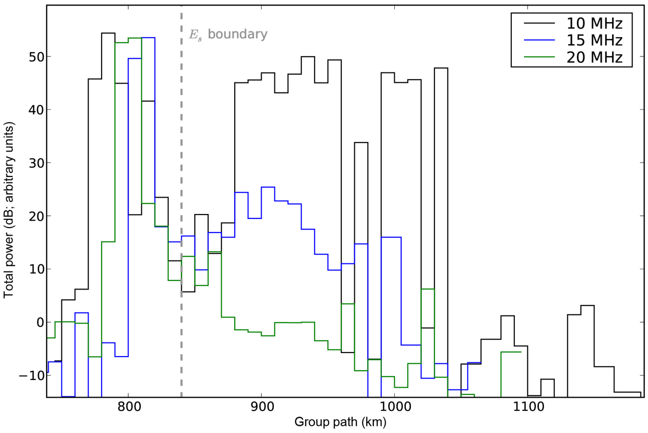

Figure 2. The total received power from WWV at LWA1 at 10, 15, and 20 MHz (black, blue, and green lines, respectively) within bins of group path over all six observing runs (see Sect. 2). The adopted group path upper boundary for E_s, 840 km (virtual height $\sim$ 170 km), is shown as a grey dashed line.

BC840 and two complementary groups without E_s detections.

3.1 *E–F* coupling

For the LWA1+WWV observations, E_s detections and non-detections were assessed based on the group path measured for the 10 MHz sky waves. The distributions of returned power within bins of group path for 10, 15, and 20 MHz are shown in Fig. 2. The 20 MHz distribution was scaled by a factor of 4 because the 20 MHz transmitter has an ERP 4 times lower than the other two (2.5 vs. 10 kW). One can see that virtually all the returned power at 15 and 20 MHz, reflections of which are (nearly) always from E_s, is at group paths below 840 km. There is a small amount of power from "two-hop" signals – those that reflect off the ionosphere, then off the ground, then off the ionosphere again – but generally, the 840 km group path provides a good cutoff to distinguish between E_s and F-region reflections at 10 MHz. Note that the linear distance between LWA1 and WWV is 770 km, implying that a group path of 840 km corresponds to a virtual height of about 170 km. This is a bit high for E_s, but one should note that this empirical limit essentially takes into account uncertainties within the group path measurements and the fact that a virtual mirror approximation is a poor representation of the often complex signal path associated with propagation through intricate E_s structures.

For the BC840 data, the 30 min average ionograms were used to determine during which time periods E_s was and was not present. Average TEC fluctuation spectral cubes were made for the four groups (two with E_s and two without), and a map of the peak spectral power over all temporal frequencies is shown for each in Fig. 3. These maps show the maximum spectral power as functions of east–west

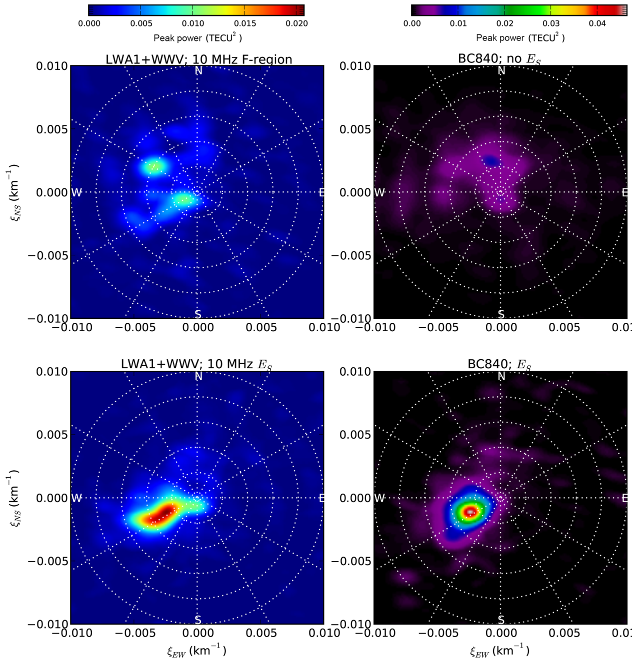

Figure 3. The peak TEC fluctuation power over all temporal frequencies from averaged power spectrum cubes generated using data from the array of the 61 GPS receivers shown in Fig. 1. The results from four different mean spectral cubes are shown: (upper left) using only GPS data from times when likely F-region reflections were detected at 10 MHz with the LWA1+WWV radar; (lower left) times when E_s reflections were detected at 10 MHz with LWA1+WWV; (upper right) times when no E_s was visible within the BC840 ionograms; and (lower right) times when E_s was apparent in the BC840 ionograms.

and north–south spatial frequencies (ξ_{EW} and ξ_{NS}). Polar grids are shown for reference at radial steps of 0.002 km^{-1}. For reference, the spectral resolution within these maps is roughly 0.0015 km^{-1} (full width at half maximum).

The two non-E_s spectra show relatively weak signatures (amplitudes $\lesssim$ 0.08 TECU) of waves moving in several directions. These include MSTIDs (wavelengths $\sim$ 250–350 km) moving westward, northwestward, northward, and northeastward and larger TIDs ($\sim$ 1000 km wavelength) moving due south. There is also a relatively weak signature of $\sim$ 1000 km wavelength TIDs moving toward the southwest seen only within the LWA1+WWV non-E_s spectral map. The fact that it is only seen within this map may be related to contamination from two-hop E_s reflections that were incorrectly flagged as F-region sky waves due to their larger group paths (see above and Fig. 2).

The two E_s maps are markedly different from their non-E_s counterparts. They both exhibit quite prominent features associated with southwestward-directed MSTIDs. Save a single, relatively weak, southward-directed, large TID feature seen in the LWA1+WWV map, these are essentially the only significant features apparent within the two maps. The main differences in these features between the two maps is that the TID feature is stronger within the BC840 map (amplitude ~ 0.22 TECU; note, the figures display fluctuation power as amplitude^2) and peaked near a single wavelength (~ 350 km). In contrast, the southwest feature in the LWA1+WWV map is distributed among a somewhat larger range of wavelengths (~ 250–500 km), with peak power corresponding to amplitudes of about 0.15 TECU. Despite these differences, the occurrences of dominant southwest-directed features within spectra corresponding to E_s detections and the virtual absence of such features within the non-E_s spectra together confirm earlier, similar results (Helmboldt, 2012; Cosgrove, 2013) that are consistent with the existence of some form of E–F coupling.

To further explore how this correlation between the appearance of E_s and F-region MSTIDs relates to the properties of the E_s layers, weighted mean spectra, similar to those shown in Fig. 3, were made using the signal amplitude at different frequencies. For the LWA1+WWV data, different mean spectra were made using the 10, 15, and 20 MHz sky wave amplitudes as weights. For the 10 MHz sky waves, only those with group paths < 840 km were used (see above). The resulting spectra are shown in the left panels of Fig. 4. From these, one can see that the TID amplitude increases with the reflection frequency and, implicitly, with E_s density. At higher frequency or density, it also appears that the MSTIDs are skewed more toward somewhat smaller wavelengths (~ 250 km). Separate mean fluctuation spectra were made using E_s signal amplitudes from the BC840 ionograms, averaged within five different frequency bins. Four evenly spaced bins were used between 1 and 6.6 MHz with the fifth bin including all E_s signals for $f > 6.6$ MHz. The first three frequency bins roughly correspond to the inferred plasma frequencies for the LWA1+WWV system at 10, 15, and 20 MHz assuming an E_s height of 110 km and a simple virtual mirror approximation. These first three bins show a similar, but more pronounced trend of increasing fluctuation power with increasing E_s frequency as is apparent from the LWA1+WWV weighted spectra. However, no comparable change in dominant wavelength is evident. Within the mean spectrum for the next highest frequency bin, 5.2–6.6 MHz, the wave amplitudes are significantly weaker, and for the largest frequency bin, the southwestward-directed MSTIDs are virtually nonexistent. This is similar to the results presented by Helmboldt (2012), which showed a decrease in MSTID activity for foEs > 3 MHz.

3.2 Meteor trails and FAIs

An analysis similar to that presented in Sect. 3.1 for the GPS-based TEC fluctuation spectra was performed on the all-sky 55.25 MHz S/N maps described in Sect. 2.1. Figure 5 shows mean S/N maps for the same E_s and non-E_s groups that are represented in Fig. 3. The region to the north

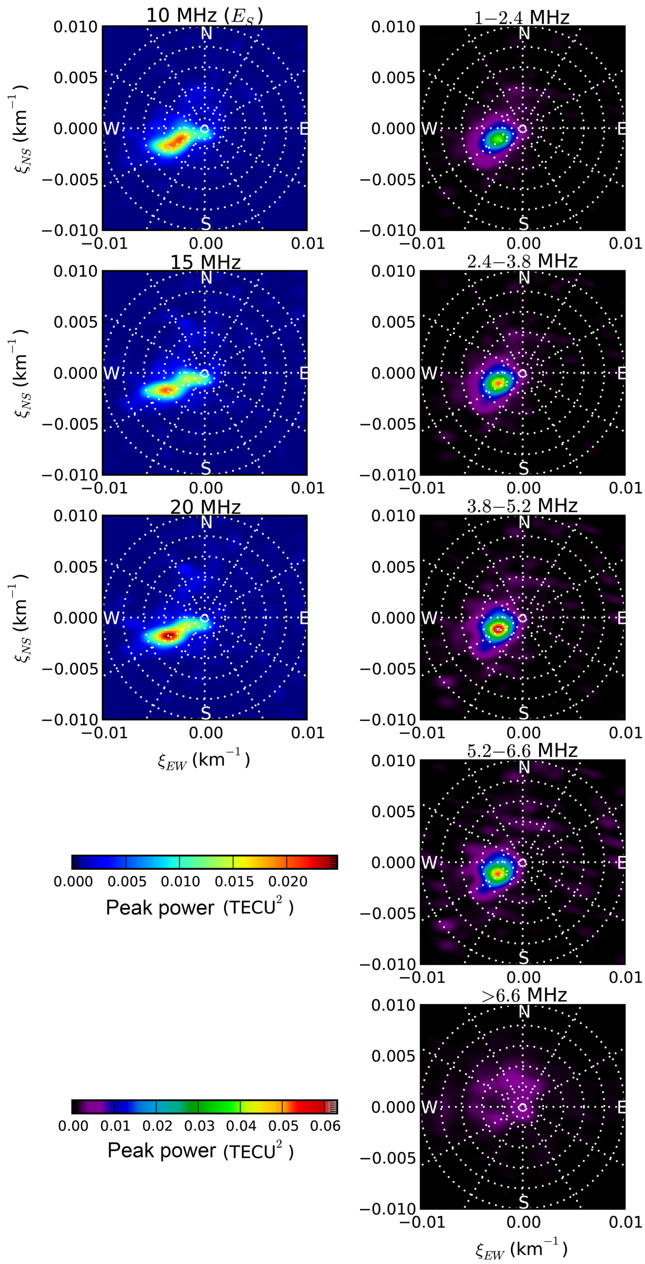

Figure 4. Similar to Fig. 3, the peak TEC fluctuation power over all temporal frequencies from averaged, GPS-based power spectrum cubes. In this case, the power spectrum cubes were generated as weighted averages where the weight was (upper left) the 10 MHz, LWA1+WWV sky wave amplitude (E_s only), (middle left) the 15 MHz LWA1+WWV amplitude, and (lower left) the 20 MHz amplitude. The panels within the right column show results from weighted mean spectral cubes, weighted with the average E_s amplitude from the BC840 ionograms within frequency bins noted above each panel.

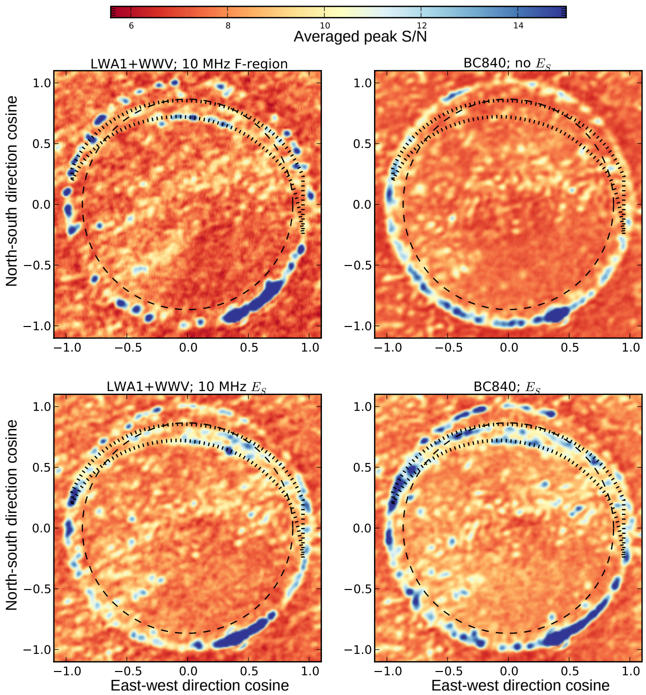

Figure 5. For the same groups of observations shown in Fig. 3, the average peak S/N map for backscattered 55.25 MHz transmissions. The region dominated by backscattering of signals from transmitters in Mexico by field-aligned irregularities (FAIs) to the north is marked by black dotted lines. This region was computed using the known transmitter location for XEPM from the FCC and heights between 90 and 130 km. An elevation of 30°, above which > 80 % of sources are meteor trails, is marked with a dashed black circle.

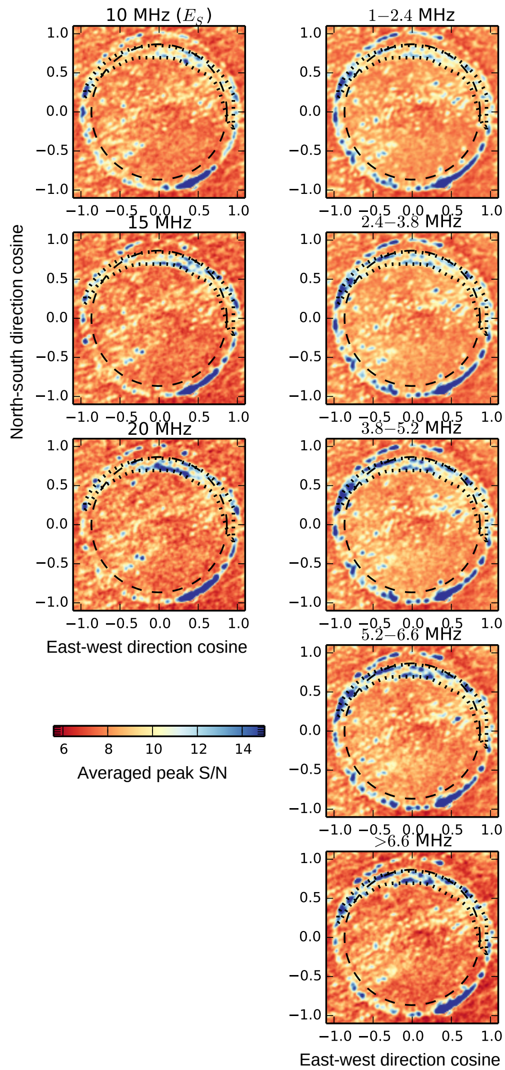

Figure 6. The weighted mean peak S/N map for scattered 55.25 MHz signals using the same weighting schemes as the corresponding panels in Fig. 4.

where backscattering by E_s FAIs is expected to be prevalent is marked in each panel with a black dotted line. This was computed using the location for XEPM obtained from the FCC (at $\phi = 31.706°$ N, $\lambda = 106.478°$ W), an assumed height range of 90–130 km, and using the international geomagnetic reference field (IRGF) parameters for the 2013 epoch. While there are certainly meteor trails detected within this region on the sky, sources within this area are excluded from meteor trail analysis due to the higher likelihood that they corresponds to FAIs.

Within the panels of Fig. 5, the circle corresponding to an elevation of 30° is marked with a black dashed line. Above this elevation, Helmboldt et al. (2014) found that >85 % of detected point-like sources at 55.25 MHz are true meteor trails, based on high-resolution time series (5.12 ms sampling) of signal amplitudes. Below this elevation limit, other transmitters and reflections off aircraft constitute a significant fraction of sources. An ongoing survey for meteor streams with LWA1 at 55.25 MHz has found that more than 90 % of sources above this limit have time series best explained by meteor trail reflections. Furthermore, this survey found a preponderance of sources within the likely FAI region in the summer of 2014 that are much longer-lived than typical meteors, consistent with E_s FAIs.

For both the LWA1- and BC840-based groups, meteor trail activity and likely FAIs were significantly more prominent when E_s was present. Like the results for MSTIDs shown in Fig. 3, this is much more pronounced within the BC840-based groups. In this case, there are few if any sources above 30° elevation (i.e., likely meteor trails) and the arcs likely associated with FAIs are not discernible at all in the mean S/N map for the non-E_s group. Specifically, the mean S/N within the FAI and meteor trail regions are 30 and 10 % larger, respectively, within the E_s map versus the non-E_s map when using BC840 data, but only 10 and 5 % higher when using LWA1 data. Again, this may point to contamination within the LWA1 non-E_s group by two-hop E_s reflections. The

FAIs that appear within these all-sky maps sometimes appear in resolved groups with elongated, wavefront-like structures. These appear to have no single dominant orientation and are generally consistent with similar observations of E_s backscatter at 30 MHz over Puerto Rico (Hysell et al., 2004; Larsen et al., 2007; Hysell et al., 2009, 2012).

Averaged 55.25 MHz S/N maps are also shown in Fig. 6, weighted by sky wave amplitudes at different frequencies. These are counterparts to the averaged TEC fluctuation spectral maps shown in Fig. 4. Here, it is evident that for both LWA1+WWV- and BC840-based averaging, both meteor trail activity and the incidence of FAIs correlate with E_s density to some degree. Specifically, the mean S/N within the meteor trail region increases by a few percent from 1.5 to 4.5 MHz. The FAI region average S/N increases by more than 10 % from 1.5 to 6 MHz. The exact dependences on f_p will be discussed more in Sect. 4.

3.3 Sporadic-E structure from passive radar

The results presented within the previous two subsections imply that up to plasma frequencies of about 5 MHz, E_s layer density increases steadily with the level of meteor activity and that this increased density may enhance E–F coupling. However, above this level, other processes must influence the structure of the E_s layers as the strength of detected MSTIDs wanes above 5 MHz and the trend between f_p and meteor activity exhibits a similar turnover. Therefore, these relatively high E_s densities cannot be explained by increased deposition of heavy ions via meteor ablation and are likely related to some process that may also disrupt E–F coupling.

To explore this further, the LWA1–WWV and BC840 data were combined to discover whether or not there is evidence for dense, isolated E_s structures that could yield high-frequency reflections but would not constitute an overall increase in the total ion content of the E_s layers. Following Helmboldt et al. (2013), we used the WWV sky waves imaged by LWA1 to localize the signals on the sky and infer the horizontal position of each E_s reflection point. This was done using the 15 MHz data since 15 MHz WWV reflections are all from E_s, which is not the case at 10 MHz, and the 15 MHz transmitter is 4 times more powerful than the one at 20 MHz. The positions were measured parallel and perpendicular to the great circle connecting the LWA1 and WWV positions at an altitude of 110 km and are plotted for each LWA1 observing run in Fig. 7, color-coded by signal amplitude. Upon visual inspection of these plots, it is clear that within a single observing run, the reflection points can be quite clustered, especially for the mid-August observing runs (DOY: 225, 233).

To quantify the level of clustering, the correlated power was computed among 15 MHz reflections within bins of horizontal separation for each observing run, then averaged into a single correlation function. This was done by multiplying the amplitude of each 15 MHz reflection by the amplitudes of all others within an observing run and then summing these products with bins of horizontal separation. This was repeated for all 15 MHz sky waves and for all observing runs and combined into a total correlation function. A normalized version of this (divided by the total over all bins) is shown in red in the panels of Fig. 8. The signals appear to be, on average, significantly correlated on horizontal scales up to about 250 km, which is not surprising given the results shown in Fig. 7. However, the correlation is significantly stronger for separations < 150 km, especially between 10 and 40 km.

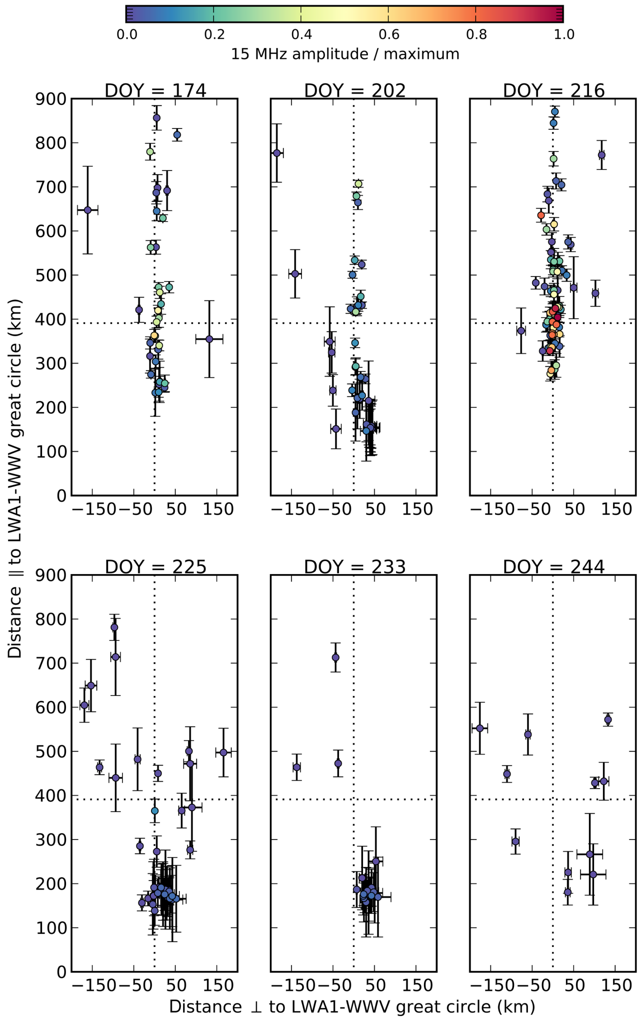

Figure 7. The horizontal locations of E_s structures reflecting 15 MHz WWV transmissions during the six observing runs. Positions are measured as arc lengths perpendicular (abscissa) and parallel (ordinate) to the great circle connecting the latitudes and longitudes of LWA1 and WWV at a height of 110 km (vertical dotted line) with LWA1 at the origin. The midpoint between LWA1 and WWV is illustrated with a horizontal dotted line. The points are color-coded according to 15 MHz sky wave amplitude; positions with ⊥ or ∥ uncertainties larger than 50 and 100 km, respectively, were excluded.

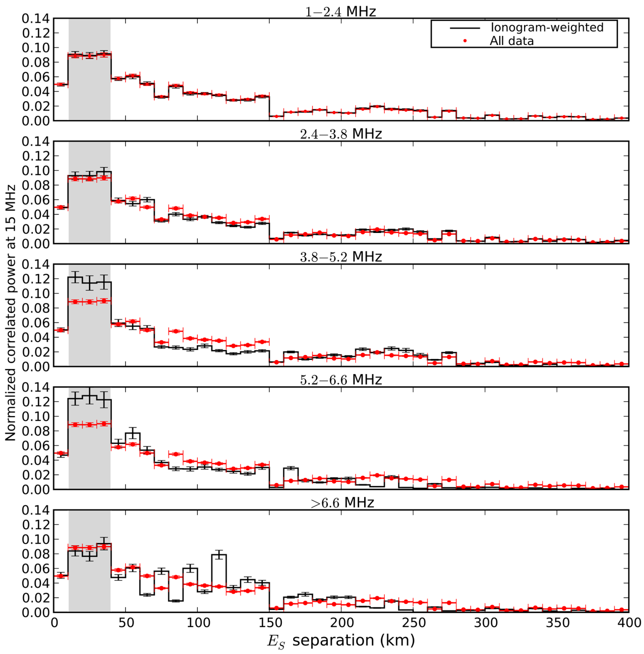

Figure 8. The mean, normalized, correlated power of 15 MHz WWV sky waves reflected by E_s within bins of horizontal separation. The correlations were measured separately for the six observing runs and then combined. The red dots show the correlation function for all 15 MHz E_s reflections. Within each panel, the black histogram shows the results if the individual correlations are weighted according to the E_s amplitudes from contemporaneous BC840 ionograms within different frequency bins. The range of separations that typically shows the strongest correlation, 10–40 km, is highlighted in grey in all panels.

To examine how this changes with E_s layer density, the correlation function was recomputed, this time weighting the correlated power from each sky wave pair by the product of the E_s signal amplitudes from the corresponding BC840 ionograms within different frequency bins. The ionogram frequency bins used were the same as those used for Figs. 4 and 6. The weighted and normalized correlation functions for these frequency bins are shown as black histograms in the panels of Fig. 8. One can see that correlation on 10–40 km scales (highlighted in grey) steadily increases with ionogram frequency up to 6.6 MHz. This is also where the backscatter S/N for FAIs peaks, implying that the 15 MHz echo clumps are associated with the same structures that host the meter-scale FAIs. Indeed, the typical distance to these FAIs from LWA1 is ~ 200 km, implying that the groups of FAIs seen within the all-sky images shown in Figs. 5–6 are consistent with sizes of a few to a few tens of kilometers.

In addition, these same size scales are consistent with wavelengths of shear instabilities thought to be the driving formation mechanism for structures associated with QP echoes (Larsen, 2000; Bernhardt, 2002). They are also consistent with the observed wavelengths of frontal structures with E_s echoes imaged at 30 MHz over Puerto Rico ($\sim$30 km; Hysell et al., 2004). Moreover, it is known that QP echoes are much more prominent within E_s layers that have substantial disparities between peak and mean densities as indicate by larger values of foEs$-$fbEs (see, e.g., Ogawa et al., 2002). For the data set presented here, the values for fbEs were relatively tightly clustered with a mean of 2.1 MHz and standard deviation of 0.5 MHz. Thus, in this case, higher values of f_p can be taken as indicators of larger peak rather than blanketing densities. This makes the proffered notion of QP predominance at higher f_p all the more plausible. However, note that the temporal sampling of the LWA1 data, one 61 ms capture every 6 min, precludes classification of these structures as bona fide QP echoes. It should be stressed that it is the size, spacing, and density of these, along with their association with E_s, that makes them similar to the known properties of structures associated with QP echoes, not their temporal variability.

4 Conclusions

The outcome of the observing campaign presented here in many ways conforms with previously published results. The preferential detection of southwestward-directed, nighttime MSTIDs during E_s has been seen before (see, e.g., Helmboldt, 2012; Cosgrove, 2013). Other authors have also demonstrated enhanced E_s during heightened meteor activity (Chandra et al., 2001; Yellaiah et al., 2001). In addition, the results from the imaging of regions of backscatter from E_s FAIs largely conforms with previous observations in the Caribbean (Hysell et al., 2004, 2009; Larsen et al., 2007). However, the intriguing component of the results shown here is the trends among metrics of these phenomena and E_s reflection/plasma frequency. This is largely made possible by the unique combination of the remote sensing platforms employed, especially the wide-band, all-sky mode of LWA1. This allows for the simultaneous detection of E_s reflections of HF transmissions from WWV, VHF backscatter by E_s FAIs, and meteor trail reflections within roughly the same geographical area.

The aforementioned trends are summarized within the panels of Fig. 9. Here, the peak TEC fluctuation power from the spectra shown in Fig. 4 is plotted versus frequency in the upper left panels. Separate plots are shown for the LWA1+WWV- and BC840-based data. The abscissa are scaled such that the WWV and BC840 frequencies match for a simple virtual mirror approximation. The prevalence of E_s FAIs, quantified by the mean 55.25 MHz S/N within the likely FAI region (marked with dotted lines in Fig. 6), is also plotted versus frequency in the middle column of panels. Similarly, the mean S/N from the 55.25 MHz maps for elevations above 30° and excluding the FAI region is used to quantify meteor trail activity as a function of f_p in the right panels. Finally, the total correlated power among WWV

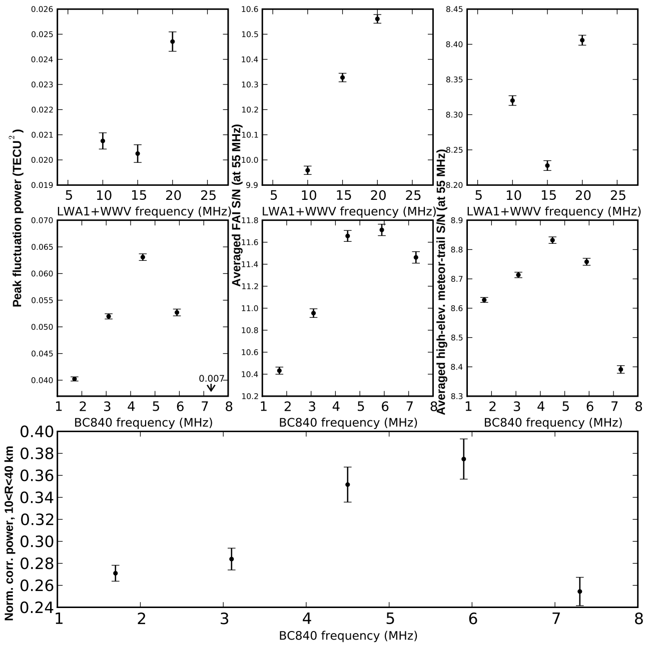

Figure 9. Several quantities plotted as functions of LWA1+WWV frequency and BC840 frequency for E_s reflections. The scales of the abscissa of the panels are set such that the LWA1+WWV and BC840 frequencies match for a simple virtual mirror approximation for the WWV reflections at a height of 110 km. The quantities plotted along the ordinates are (left column) peak TEC fluctuation power from the spectral maps shown in Fig. 4, (middle column) the average peak S/N at 55.25 MHz for FAIs (see Fig. 5 and Sect. 2.1), (right column) the average peak S/N for high-elevation (>30°) 55.25 MHz reflections, which are dominated by meteor trails (>80 %; see Sect. 2.1), and (lower panel) the normalized correlated power from 15 MHz WWV sky waves on horizontal separations between 10 and 40 km (see Fig. 8).

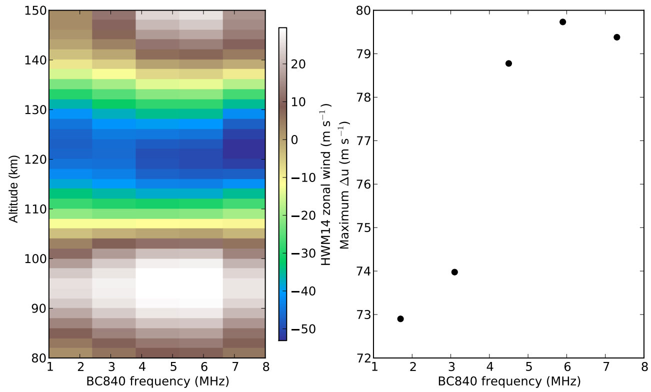

Figure 10. Left: the mean zonal wind profile computed with HWM14, weighted by BC840 ionogram E_s amplitude for five different bins of f_p; right: the difference between maximum and minimum zonal wind for each f_p bin.

15 MHz reflection points on horizontal scales between 10 and 40 km (see Sect. 3.3 and Fig. 8) is plotted versus BC840 E_s frequency in the bottom panel of Fig. 9.

Both the TEC fluctuation power and meteor trail S/N correlate with f_p up to about 4.5 MHz. Beyond this limit, both trends turn over and drop substantially above 6 MHz. The FAI S/N and correlated power at 15 MHz on 10–40 km scales are both likewise correlated with f_p. However, the trends for these two quantities remain up to higher frequencies, roughly up to 6 MHz. After this, the trends turn over, less dramatically so for the FAIs. As discussed in Sect. 3, this is consistent with the 15 MHz echo clumps corresponding to the regions that contain the backscattering FAIs and with known properties of QP echoes.

The observations presented here clearly show that southwestward propagating MSTIDs are more common when E_s is present. By themselves, these findings cannot rule out the possibility that there is no causal relationship between these two phenomena and that they are simply both affected by the same set of underlying circumstances (e.g., the presence of wind-modulated gravity waves). However, the clear trend between MSTID amplitude and E_s plasma frequency strongly implies a physical connection between the two. This connection seems to break down above $f_p \simeq 4.5$ MHz, as does the correlation between f_p and meteor activity. It is above this f_p limit where structures consistent with QP echoes are most prominent within both the 55.25 and 15 MHz data. While there have been recent observations of concomitant MSTIDs and QP echoes (Hysell et al., 2010; Helmboldt et al., 2012), this investigation seems to indicate that these are the exception rather than the rule.

The results of this work appear to intimate that whatever physical mechanism may tie together E_s and MSTIDs must work more most efficiently with a kind of classical or quiescent E_s layer. In other words, the canonical scenario for E_s formation starts with metallic ions, deposited by ablating meteors, which are compressed into a stable and thin layer by opposing Lorentz forces within a portion of the E region where the zonal wind has a negative vertical gradient. Within this formation picture, one would expect the density of such a layer to be correlated with the level of meteor activity, which it appears to be up to $f_p \simeq 4.5$ MHz.

Once such a layer has formed, if shear instabilities begin to grow, the quasi-uniform layer can be redistributed into a region of clumps and voids, similar to what Bernhardt (2002) found when calculating the impact of neutral-gas K–H instabilities on E_s layers. In this case, the peak density of the region would depend more on the efficiency of the shear instabilities to form dense clumps than the amount of meteor-deposited heavy ions. Thus, for E_s regions with large peak densities, the correlation between f_p and meteor activity would break down and dense clumps would become more prevalent. This is precisely what was observed within the investigation presented here.

This basic paradigm is partially supported by the quiet-time lower thermospheric wind conditions as described by the updated Horizontal Wind Model (HWM14; Drob et al., 2015). While HWM14 provides only an empirically driven, climatological representation of winds within the thermosphere and not actual measurements, it can still be used to explore how the expected neutral wind conditions within the E region change with E_s properties. HWM14 was used to compute the zonal wind profile between 80 and 150 km altitude near the location of LWA1 at the midpoint of each 30 min window used to compute the mean BC840 ionograms (see Sect. 2.2). Weighted averages of the profiles were then computed as a function of f_p in the same manner as was used for the TEC fluctuation spectra and the 55.25 MHz all-sky images (see Sect. 3.1–3.2 and Figs. 4, 6). The profiles are shown as an image in the left panel of Fig. 10. The semidiurnal-tide driven zonal wind shears expected for times when E_s is present are apparent for all values of f_p. The magnitude of the shear appears to increase with f_p up to about 5–6 MHz. This is better visualized within the right panel of Fig. 10 where the difference between the maximum and minimum zonal wind is plotted as a function of f_p. The pattern within this plot is quite similar to that seen for FAI backscatter S/N as a function of f_p (see Fig. 9), implying that more dense groups of FAIs tend to occur at times when the zonal wind shear is expected to be more pronounced. This is consistent with the notion that these dense structures result from shear instabilities.

It should be noted that the results of this investigation are also essentially consistent with simulations of the coupled E–F instability described by Cosgrove et al. (2004). Three-dimensional simulations performed by Yokoyama et al. (2009) and Yokoyama and Hysell (2010) showed that when starting with a quiescent, stable E_s layer, northwest-to-southeast aligned wavefronts form within both the E_s layer and in the F region via the coupled instability. This happens even when starting with a set of random perturbations as the instability preferentially grows disturbances aligned in this way. However, the irregularities reach a relatively stable perturbation amplitude of a few percent within about 30 min or less, leaving the original, smooth E_s layer largely intact. Thus, while the structures formed within these simulations have wavelengths ~ 30 km, it seems unlikely that the dense, relatively isolated structures observed to coincide with QP echoes are formed in this way.

In fact, given the results presented here, it appears more likely that, as previously asserted (see, e.g., Larsen, 2000), these very dense structures result from shear instabilities that significantly disrupt the otherwise relatively smooth E_s layer. Such disruptions would compromise the efficiency of the interaction between polarized electric fields with the E_s and F regions and could explain why MSTID activity quickly vanishes for $f_p > 5$ MHz. However, it should be noted that the effectiveness of the Cosgrove et al. (2004) instability depends as much on the integrated Pedersen and Hall conductivities within the F region and E_s layer, respectively, as it does on E_s layer density (see Cosgrove and Tsunoda, 2002; Cosgrove et al., 2004; Yokoyama et al., 2004). Therefore, the E_s layer density for which MSTID activity peaks may depend significantly on solar activity and may not be universally at $f_p \sim 4$–5 MHz.

Data availability

The unprocessed GPS data used in this investigation are publicly available in compressed RINEX format via anonymous FTP from the two databases listed in Sect. 2.2. The digisonde data for BC840 was obtained from the DIDBase repository (DIDBase, available at: http://ulcar.uml.edu/DIDBase/; Reinisch et al., 2004). Processed data, including fluctuation spectra, are available upon request to the author. Raw LWA1 data are proprietary and are not publicly available. However, all-sky images and image cubes generated from these data for this manuscript can be made available upon request to the author.

Acknowledgements. The author would like to thank the reviewers for useful comments and suggestions. The author would also like to thank D. Drob for providing code for running the HWM14 model. Basic research at the Naval Research Laboratory is supported by 6.1 base funding. Construction of the LWA has been supported by the Office of Naval Research under Contract N00014-07-C=0147. Support for operations and continuing development of the LWA1 is provided by the National Science Foundation under grant AST-1139963 and AST-1139974 of the University Radio Observatory program.

The topical editor, K. Hosokawa, thanks two anonymous referees for help in evaluating this paper.

References

Arras, C., Jacobi, C., Wickert, J., Heise, S., and Schmidt, T.: Sporadic E signatures revealed from multi-satellite radio occultation measurements, Adv. Radio Sci., 8, 225–230, doi:10.5194/ars-8-225-2010, 2010.

Baggaley, W. J. and Steel, D. I.: The seasonal structure of ionosonde sporadic-E parameters and meteoroid deposition rates, Plan. Space Sci., 32, 1533–1539, doi:10.1016/0032-0633(84)90021-7, 1984.

Bernhardt, P. A.: The modulation of sporadic-E layers by Kelvin–Helmholtz billows in the neutral atmosphere, J. Atmos. Sol.-Terr. Phy., 64, 1487–1504, doi:10.1016/S1364-6826(02)00086-X, 2002.

Bowman, G. G.: Quasi-periodic scintillations at mid-latitudes and their possible association with ionospheric sporadic-E structures, Ann. Geophys., 7, 259–267, 1989.

Chandra, H., Sharma, S., Devasia, C. V., Subbarao, K. S. V., Sridharan, R., Sastri, J. H., and Rao, J. V. S. V.: Sporadic-E associated with the Leonid meteor shower event of November 1998 over low and equatorial latitudes, Ann. Geophys., 19, 59–69, doi:10.5194/angeo-19-59-2001, 2001.

Cosgrove, R.: Mechanisms for E-F coupling and their manifestation, J. Atmos. Sol.-Terr. Phy., 103, 56–65, doi:10.1016/j.jastp.2013.03.011, 2013.

Cosgrove, R. B.: Generation of mesoscale *F* layer structure and electric fields by the combined Perkins and E_S layer instabilities, in simulations, Ann. Geophys., 25, 1579–1601, doi:10.5194/angeo-25-1579-2007, 2007.

Cosgrove, R. B. and Tsunoda, R. T.: A direction-dependent instability of sporadic-*E* layers in the nighttime midlatitude ionosphere, Geophys. Res. Lett. 29, 1864, doi:10.1029/2002GL014669, 2002.

Cosgrove, R. B., Tsunoda, R. T., Fukao, S., and Yamamoto, M.: Coupling of the Perkins instability and the sporadic *E* layer instability derived from physical arguments, J. Geophys. Res.-Space, 109, A06301, doi:10.1029/2003JA010295, 2004.

Dowell, J., Wood, D., Stovall, K., Ray, P. S., Clarke, T., and Taylor, G.: The Long Wavelength Array Software Library, J. Astron. Instrum., 1, 1250006, doi:10.1142/S2251171712500067, 2012.

Drob, D. P., Emmert, J. T., Meriwether, J. W., Makela, J. J., Doornbos, E., Conde, M., Hernandez, G., Noto, J., Zawdie, K. A., McDonald, S. E., Huba, J. D., and Klenzing, J. H.: An update to the Horizontal Wind Model (HWM): The quiet time thermosphere, Earth Space Sci., 2, 301–319, doi:10.1002/2014EA000089, 2015.

Ellingson, S. W., Taylor, G. B., Craig, J., Hartman, J., Dowell, J., Wolfe, C. N., Clarke, T. E., Hicks, B. C., Kassim, N. E., Ray, P. S., Rickard, L. J., Schinzel, F. K., and Weiler, K. W.: The LWA1 Radio Telescope, IEEE T. Antenn. Propag., 61, 2540–2549, doi:10.1109/TAP.2013.2242826, 2013.

Haldoupis, C.: Midlatitude Sporadic E. A Typical Paradigm of Atmosphere-Ionosphere Coupling, Space Sci. Rev., 168, 441–461, doi:10.1007/s11214-011-9786-8, 2012.

Haldoupis, C., Pancheva, D., Singer, W., Meek, C., and MacDougall, J.: An explanation for the seasonal dependence of midlatitude sporadic E layers, J. Geophys. Res.-Space, 112, A06315, doi:10.1029/2007JA012322, 2007.

Helmboldt, J. F.: Insights into the nature of northwest-to-southeast aligned ionospheric wavefronts from contemporaneous Very Large Array and ionosonde observations, J. Geophys. Res.-Space, 117, A07310, doi:10.1029/2012JA017802, 2012.

Helmboldt, J. F. and Intema, H. T.: Advanced spectral analysis of ionospheric waves observed with sparse arrays, J. Geophys. Res.-Space, 119, 1392–1413, doi:10.1002/2013JA019162, 2014.

Helmboldt, J. F., Lazio, T. J. W., Intema, H. T., and Dymond, K. F.: A new technique for spectral analysis of ionospheric TEC fluctuations observed with the Very Large Array VHF system: From QP echoes to MSTIDs, Radio Sci., 47, RS0L02, doi:10.1029/2011RS004787, 2012.

Helmboldt, J. F., Clarke, T. E., Craig, J., Dowell, J. D., Ellingson, S. W., Hartman, J. M., Hicks, B. C., Kassim, N. E., Taylor, G. B., and Wolfe, C. N.: Passive all-sky imaging radar in the HF regime with WWV and the first station of the Long Wavelength Array, Radio Sci., 48, 491–512, doi:10.1002/rds.20056, 2013.

Helmboldt, J. F., Ellingson, S. W., Hartman, J. M., Lazio, T. J. W., Taylor, G. B., Wilson, T. L., and Wolfe, C. N.: All-sky imaging of meteor trails at 55.25 MHz with the first station of the Long Wavelength Array, Radio Sci., 49, 157–180, doi:10.1002/2013RS005220, 2014.

Hernández-Pajares, M., Juan, J. M., and Sanz, J.: Medium-scale traveling ionospheric disturbances affecting GPS measurements: Spatial and temporal analysis, J. Geophys. Res.-Space, 111, A07S11, doi:10.1029/2005JA011474, 2006.

Hicks, B. C., Paravastu-Dalal, N., Stewart, K. P., Erickson, W. C., Ray, P. S., Kassim, N. E., Burns, S., Clarke, T., Schmitt, H., Craig, J., Hartman, J., and Weiler, K. W.: A Wide-Band, Active Antenna System for Long Wavelength Radio Astronomy, Pub. Astro. Soc. Pac., 124, 1090–1104, doi:10.1086/668121, 2012.

Hocking, W. K., Fuller, B., and Vandepeer, B.: Real-time determination of meteor-related parameters utilizing modern digital technology, J. Atmos. Sol.-Terr. Phy., 63, 155–169, doi:10.1016/S1364-6826(00)00138-3, 2001.

Hysell, D. L., Larsen, M. F., and Zhou, Q. H.: Common volume coherent and incoherent scatter radar observations of mid-latitude sporadic *E*-layers and QP echoes, Ann. Geophys., 22, 3277–3290, doi:10.5194/angeo-22-3277-2004, 2004.

Hysell, D. L. and Burcham, J. D.: HF radar observations of quasiperiodic E layer echoes over North America, J. Geophys. Res., 104, 4361–4372, doi:10.1029/1998JA900144, 1999.

Hysell, D. L., Nossa, E., Larsen, M. F., Munro, J., Sulzer, M. P., and González, S. A.: Sporadic E layer observations over Arecibo using coherent and incoherent scatter radar: Assessing dynamic stability in the lower thermosphere, J. Geophys. Res.-Space, 114, A12303, doi:10.1029/2009JA014403, 2009.

Hysell, D. L., Yokoyama, T., Nossa, E., Hedden, R. B., Larsen, M. F., Munro, J., Smith, S., Sulzer, M. P., and Gonzàlez, S. A.: Radar and optical observations of irregular midlatitude sporadic *E* layers beneath MSTIDs, in: Aeronomy of the Earth's Atmosphere and Ionosphere, edited by: Hultqvist, B., Abdu, M. A., Pacheva, D., and Bhattacharyya, A., IAGA Special Sopron Book Series, 2010.

Hysell, D. L., Nossa, E., Larsen, M. F., Munro, J., Smith, S., Sulzer, M. P., and GonzáLez, S. A.: Dynamic instability in the lower thermosphere inferred from irregular sporadic E layers, J. Geophys. Res.-Space, 117, A08305, doi:10.1029/2012JA017910, 2012.

Larsen, M. F.: A shear instability seeding mechanism for quasiperiodic radar echoes, J. Geophys. Res., 105, 24931–24940, doi:10.1029/1999JA000290, 2000.

Larsen, M. F., Hysell, D. L., Zhou, Q. H., Smith, S. M., Friedman, J., and Bishop, R. L.: Imaging coherent scatter radar, incoherent scatter radar, and optical observations of quasiperiodic structures associated with sporadic *E* layers, J. Geophys. Res.-Space, 112, A06321, doi:10.1029/2006JA012051, 2007.

Miller, K. L. and Smith, L. G.: Incoherent scatter radar observations of irregular structure in mid-latitude sporadic *E* layers, J. Geophys. Res., 83, 3761–3775, doi:10.1029/JA083iA08p03761, 1978.

Nelson, G. K., Lombardi, M. A., and Okayama, D. T.: NIST time and frequency radio stations: WWV, WWVH, and WWVB, NIST Special Publication, 250–267, 2005.

Ogawa, T., Takahashi, O., Otsuka, Y., Nozaki, K., Yamamoto, M., and Kita, K.: Simultaneous middle and upper atmosphere radar and ionospheric sounder observations of midlatitude E region irregularities and sporadic *E* layer, J. Geophys. Res.-Space, 107, 1275, doi:10.1029/2001JA900176, 2002.

Pan, C. J. and Tsunoda, R. T.: Quasi-periodic echoes observed with the Chung-Li VHF Radar during the SEEK Campaign, Geophys. Res. Lett., 25, 1809–1812, doi:10.1029/98GL00302, 1998.

Perkins, F.: Spread *F* and ionospheric currents, J. Geophys. Res., 78, 218–226, doi:10.1029/JA078i001p00218, 1973.

Reinisch, B. W., Galkin, I. A., Khmyrov, G., Kozlov, A., and Kitrosser, D.: Automated collection and dissemination of ionospheric data from the digisonde network, Adv. Radio Sci., 2, 241–247, 2004.

Taylor, G. B., Ellingson, S. W., Kassim, N. E., Craig, J., Dowell, J., Wolfe, C. N., Hartman, J., Bernardi, G., Clarke, T., Cohen, A., Dalal, N. P., Erickson, W. C., Hicks, B., Greenhill, L. J., Jacoby, B., Lane, W., Lazio, J., Mitchell, D., Navarro, R., Ord, S. M., Pihlström, Y., Polisensky, E., Ray, P. S., Rickard, L. J., Schinzel, F. K., Schmitt, H., Sigman, E., Soriano, M., Stewart, K. P., Stovall, K., Tremblay, S., Wang, D., Weiler, K. W., White, S., and Wood, D. L.: First Light for the First Station of the Long Wavelength Array, J. Astron. Instrum., 1, 1250004, doi:10.1142/S2251171712500043, 2012.

Tolman, B., Harris, R. B., Gaussiran, T., Munton, D., Little, J., Mach, R., Nelsen, S., and Renfro, B.: The GPS Toolkit: Open Source GPS Software, 16th International Technical Meeting of the Satellite Division of the Institute of Navigation, Long Beach, California, 9–12 September 2003, 2004.

Tsugawa, T., Otsuka, Y., Coster, A. J., and Saito, A.: Medium-scale traveling ionospheric disturbances detected with dense and wide TEC maps over North America, Geophys. Res. Lett., 34, L22101, doi:10.1029/2007GL031663, 2007.

Webster, A. R., Brown, P. G., Jones, J., Ellis, K. J., and Campbell-Brown, M.: Canadian Meteor Orbit Radar (CMOR), Atmos. Chem. Phys., 4, 679–684, doi:10.5194/acp-4-679-2004, 2004.

Whitehead, J. D.: Recent work on mid-latitude and equatorial sporadic-E, J. Atmos. Terr. Phys., 51, 401–424, 1989.

Yellaiah, G., Suresh, K., and Raghavender, B.: Study of Es occurrences during meteor shower periods at Hyderabad by using FM radio signals, B. Astron. Soc. India, 29, 251–257, 2001.

Yokoyama, T. and Hysell, D. L.: A new midlatitude ionosphere electrodynamics coupling model (MIECO): Latitudinal dependence and propagation of medium-scale traveling ionospheric disturbances, Geophys. Res. Lett., 37, L08105, doi:10.1029/2010GL042598, 2010.

Yokoyama, T., Horinouchi, T., Yamamoto, M., and Fukao, S.: Modulation of the midlatitude ionospheric E region by atmospheric gravity waves through polarization electric field, J. Geophys. Res.-Space, 109, A12307, doi:10.1029/2004JA010508, 2004.

Yokoyama, T., Hysell, D. L., Otsuka, Y., and Yamamoto, M.: Three-dimensional simulation of the coupled Perkins and E_s-layer instabilities in the nighttime midlatitude ionosphere, J. Geophys. Res.-Space, 114, A03308, doi:10.1029/2008JA013789, 2009.